Supplement of Atmos. Chem. Phys., 26, 6449–6470, 2026
https://doi.org/10.5194/acp-26-6449-2026-supplement

Atmospheric Chemistry and Physics
Open Access
EGU

Supplement of

Variability of ice supersaturated regions at flight altitudes: evaluation of ERA5 reanalysis using IAGOS in situ measurements

Katarina Grubbe Hildebrandt et al.

Correspondence to: Katarina Grubbe Hildebrandt (k.g.hildebrandt@tudelft.nl) and Feijia Yin (f.yin@tudelft.nl)

S1 Sensitivity to definition of cloudy and clear-sky conditions

Different definitions have been presented to distinguish between cloud free and cloudy conditions. Wolf et al. (2025) used the ice crystal number concentration to differentiate these conditions in IAGOS and the cloud cover (CC) in ERA5. Sanogo et al. (2024) also used the ice crystal number concentration to determine if an IAGOS measurement point was within cloudy, clear-sky or indeterminate conditions. Wang et al. (2025) used the cloud ice water content (CIWC) to distinguish between cloudy and clear-sky in both IAGOS and ERA5. Recently, Petzold et al. (2025) published a methodology using the CIWC to indicate in-cloud conditions, separating the conditions into clear-sky, subvisible cirrus and visible cirrus based on specified CIWC thresholds. Here, we analyse the sensitivity of using different definitions.

First, we analyse the impact of using the ice crystal number concentration to classify in-cloud conditions in the IAGOS dataset, and the CIWC thresholds from Wang et al. (2025) to distinguish between cloudy and cloud-free conditions in ERA5. The results for the extratropic and tropic regions are shown in Fig. S1 and Fig. S2. At RHi values below 50%, there is good agreement between IAGOS and ERA5 under clear-sky conditions in most regions, with the exception of North America UT and Southern Trans-Pacific UT. When using the CC definition for ERA5, we saw good agreement between 0 and 75%. In all regions, the probability of ice supersaturation in ERA5 under clear-sky conditions defined by the CIWC is lower compared to clear-sky conditions defined by the CC in the UT and TROP. In the tropics, ERA5 shows little to no ice supersaturation in the UT under clear-sky conditions when using the CIWC thresholds from Wang et al. (2025), although the IAGOS measurements show that this is possible. Under cloudy conditions, the magnitude and shape of the PDFs differ between IAGOS and ERA5 in the extratropical TROP and UT and tropical UT. ERA5 displays a distinct plateau between RHi values of 0 and 100%, with a pronounced peak at 100%. This plateau was not observed with the CC definition. Meanwhile, the IAGOS PDF increases more gradually from approximately 25% until its peak, which is generally above 100%; this peak is also still observed at 100% in ERA5.

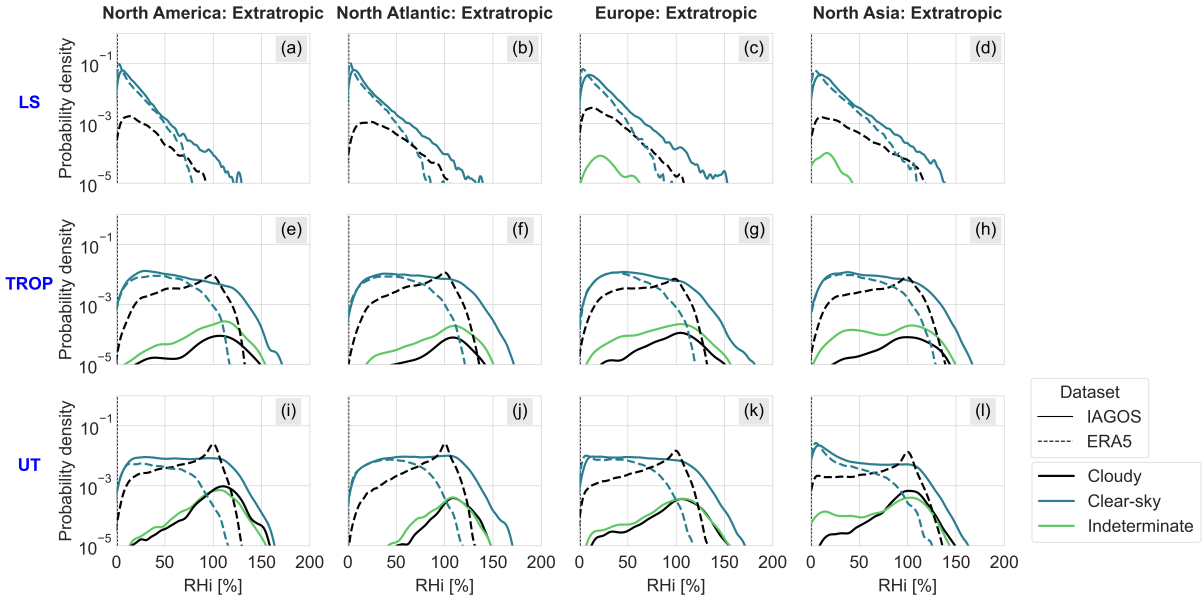

Figure S1. (a-l) Probability density function of IAGOS and ERA5 relative humidity over ice in the upper troposphere (UT), at the tropopause (TROP) and in the lower stratosphere (LS) for cloudy, clear-sky and indeterminate conditions (only IAGOS) in the four extratropic regions. For ERA5, clear-sky is defined as CIWC $= 0$ and cloudy as CIWC > 0 as per the definition from Wang et al. (2025). For IAGOS, we still distinguish between the three conditions using the ice crystal number concentration. The PDFs per subplot are normalised with respect to the number of observations within each subset of IAGOS or ERA5 used for that subplot. Only regions and atmospheric layers with 250+ samples are considered.

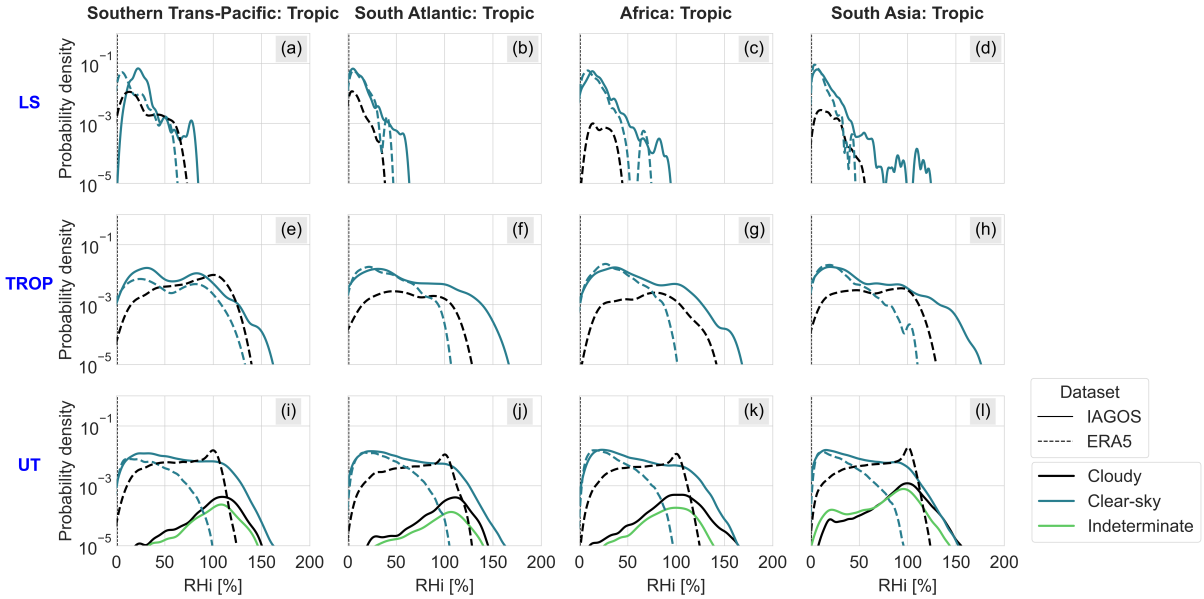

Figure S2. (a-l) Probability density function of IAGOS and ERA5 relative humidity over ice in the upper troposphere (UT), at the tropopause (TROP) and in the lower stratosphere (LS) for cloudy, clear-sky and indeterminate conditions (only IAGOS) in the four tropic regions. For ERA5, clear-sky is defined as CIWC $= 0$ and cloudy as CIWC > 0 as per the definition from Wang et al. (2025). For IAGOS, we still distinguish between the three conditions using the ice crystal number concentration. The PDFs per subplot are normalised with respect to the number of observations within each subset of IAGOS or ERA5 used for that subplot. Only regions and atmospheric layers with 250+ samples are considered.

We also investigated the impact of using the ice crystal number concentration in IAGOS to classify in-cloud conditions in the IAGOS dataset, and the CIWC thresholds based on Petzold et al. (2025) to classify cloudy conditions in ERA5. We make the assumption that 1 ppmv = $6.2 \cdot 10^{-7}$ kg/kg using molar mass conversion as we have no information on the mass of moist air, which is used within the CIWC definition. The results can be seen in Fig. S3 for the extratropic regions. The tropic regions are not shown as with this definition because there is no significant change in the ERA5 PDF under clear-sky conditions compared to using the threshold of Wang et al. (2025), although its effect can also be seen in Fig. S5. However, now that an indeterminate category is defined using the CIWC, the plateau previously seen in Fig. S1 and Fig. S2 under cloudy conditions is less distinguishable. The cloudy condition still shows pronounced peaks at RHi = 100% in ERA5.

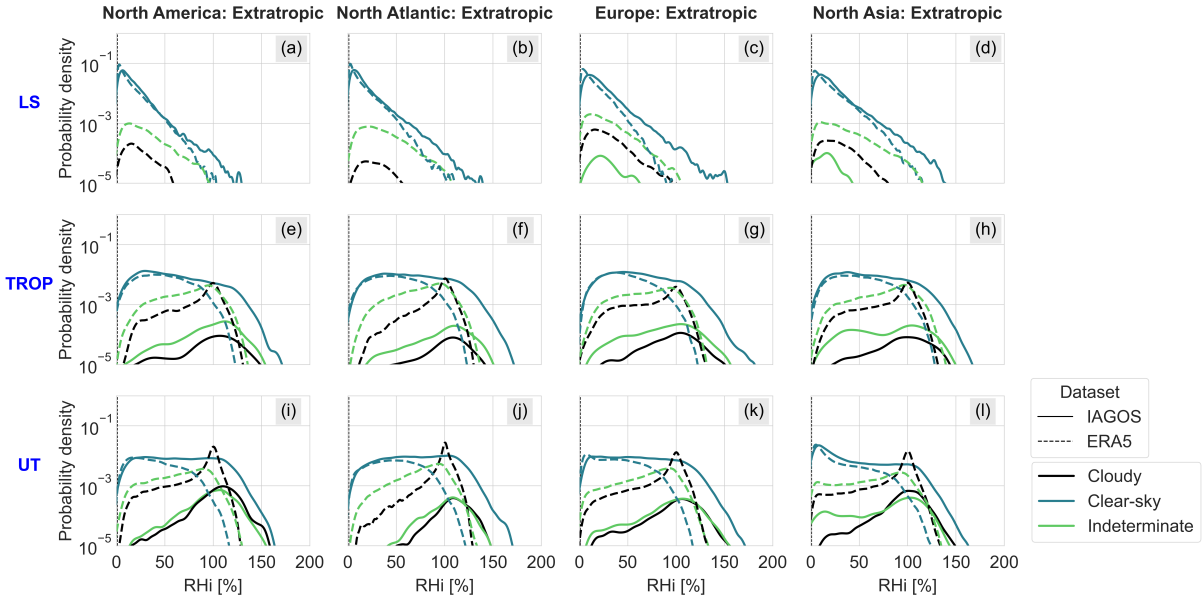

Figure S3. (a-l) Probability density function of IAGOS and ERA5 relative humidity over ice in the upper troposphere (UT), at the tropopause (TROP) and in the lower stratosphere (LS) for cloudy, clear-sky and indeterminate conditions in the four extratropic regions. For ERA5, clear-sky is defined as CIWC $< 6.2 \cdot 10^{-10}$, cloudy as CIWC $\geq 6.2 \cdot 10^{-7}$ and indeterminate as $6.2 \cdot 10^{-10} \leq$ CIWC $< 6.2 \cdot 10^{-7}$. For IAGOS, we still distinguish between the three conditions using the ice crystal number concentration. The PDFs per subplot are normalised with respect to the number of observations within each subset of IAGOS or ERA5 used for that subplot. Only regions and atmospheric layers with 250+ samples are considered.

The previous comparisons only looked at sensitivities to changing the cloudy and clear-sky definitions for ERA5. However, given that Wang et al. (2025) and Petzold et al. (2025) also used the CIWC for IAGOS, we looked at the differences when using the same definition for IAGOS and ERA5. In Fig. S4 and Fig. S5, we consider the PDF of IAGOS and ERA5 using the CIWC thresholds from Petzold et al. (2025). Using this definition for both IAGOS and ERA5 shows an overall better agreement in the RHi distribution for clear-sky, indeterminate and cloudy conditions. This is because the CIWC excludes subvisible cirrus from clear-sky conditions in both ERA5 and IAGOS, reducing the limitations introduced by the IAGOS Backscatter Cloud Probe (BCP), which can miss very thin clouds. Using the CIWC, however, still reveals issues in the prediction of ice supersaturation conditions in ERA5; in clear-sky conditions, ice supersaturation is still underestimated and the distinct peak in the RHi distribution under cloudy conditions due to the saturation adjustment is still present.

The main difference between the ice crystal number concentration, the CC and the CIWC definition is how the data points are classified. With the ice crystal number concentration and the CC definition, more points are classified as clear-sky compared to the CIWC definition, as the CIWC tends to classify measurements as in-cloud if there is any sign of the presence of ice clouds. This results in a lower probability of observable ice supersaturation conditions in clear-sky conditions when using the CIWC definition, also confirmed by Wang et al. (2025) and Petzold et al. (2025). As an example, the IAGOS ISSR fraction in the North Atlantic under clear-sky conditions, found with the ice crystal number concentration, shows a maximum of approximately 25% at 30 hPa below the tropopause. However, with the CIWC definition, this maximum is 5%. For contrail avoidance purposes, the distinction between clear-sky and subvisible cirrus is not critical because contrail cirrus would result in a warming impact in both cases (Petzold et al., 2025). Therefore, maintaining the ice crystal number concentration in IAGOS as the observational reference, we recommend using the cloud cover in ERA5 to distinguish between cloudy and clear-sky conditions. The thresholds for the CIWC could be adjusted to reduce the number of points classified as in-cloud, but determining the optimal threshold would require further investigation.

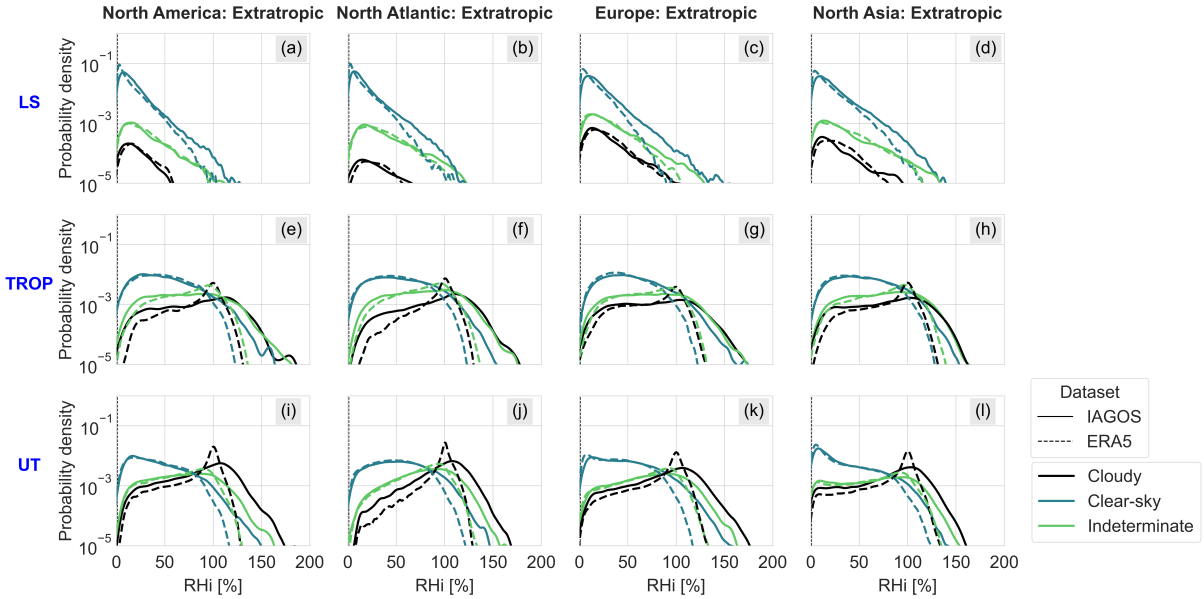

Figure S4. (a-l) Probability density function of IAGOS and ERA5 relative humidity over ice in the upper troposphere (UT), at the tropopause (TROP) and in the lower stratosphere (LS) for cloudy, clear-sky and indeterminate conditions in the four tropic regions. Clear-sky is defined as CIWC $< 6.2 \cdot 10^{-10}$, cloudy as CIWC $\geq 6.2 \cdot 10^{-7}$ and indeterminate as $6.2 \cdot 10^{-10} \leq$ CIWC $< 6.2 \cdot 10^{-7}$. The PDFs per subplot are normalised with respect to the number of observations within each subset of IAGOS or ERA5 used for that subplot. Only regions and atmospheric layers with 250+ samples are considered.

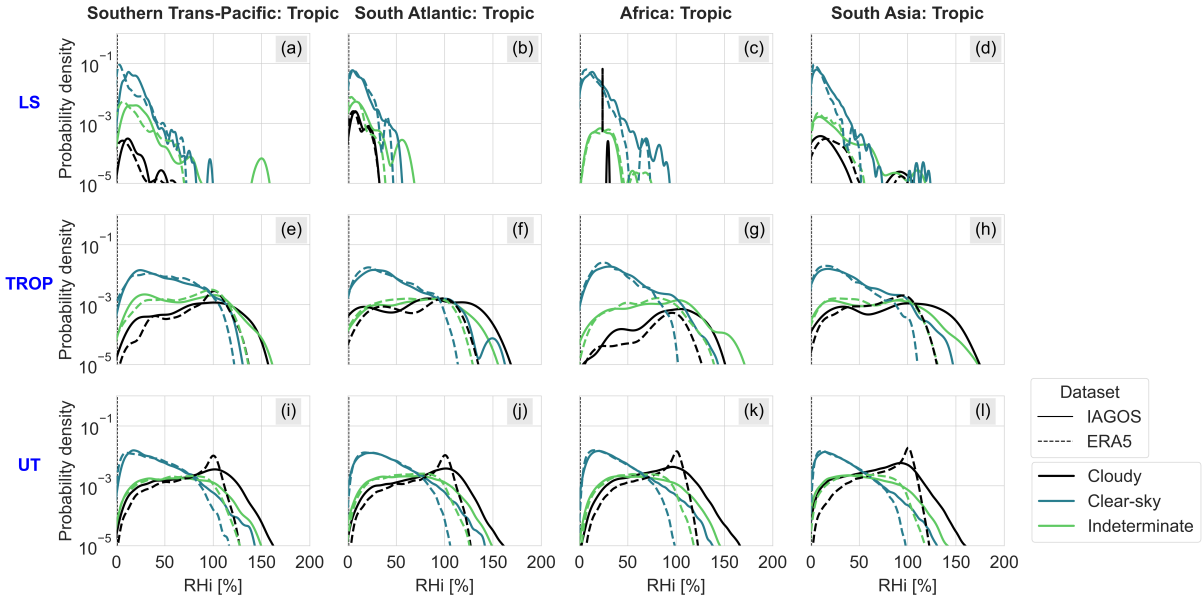

Figure S5. (a-l) Probability density function of IAGOS and ERA5 relative humidity over ice in the upper troposphere (UT), at the tropopause (TROP) and in the lower stratosphere (LS) for cloudy, clear-sky and indeterminate conditions in the four tropic regions. Clear-sky is defined as CIWC $< 6.2 \cdot 10^{-10}$, cloudy as CIWC $\geq 6.2 \cdot 10^{-7}$ and indeterminate as $6.2 \cdot 10^{-10} \leq$ CIWC $< 6.2 \cdot 10^{-7}$. The PDFs per subplot are normalised with respect to the number of observations within each subset of IAGOS or ERA5 used for that subplot. Only regions and atmospheric layers with 250+ samples are considered.

S2 Effect of sample size on results

The evaluation of ERA5 using IAGOS is highly dependent on the number of available measurements from IAGOS. If we do not have enough measurements, our conclusions may not be representative. Hence, in this appendix, we explore the effect of the sample size on temperature, relative humidity over ice (RHi), the ice supersaturated region (ISSR) fraction, and the equitable threat score (ETS).

The effect of the sample size on temperature and RHi is shown in Fig. S6 and Fig. S7, respectively. A maximum sample size of 2000 was chosen due to stabilisation of mean and standard deviation and 1000 tests were drawn in total for all sample sizes based on literature (Johnson, 2001). We see that as the number of sample size increases, the standard deviation decreases. At a sample size of 100, we find that the mean plus or minus 1 standard deviation is within the accuracy range of the IAGOS ICH sensor. The mean appears to stabilise at around 250 to 500 samples. However, from 500 samples on, the standard deviation range also seems to stabilise, but this is already within the accuracy range. Hence, for the evaluation of mean temperature and RHi, it is recommended to use at least 250 to 500 samples for a given region and vertical level.

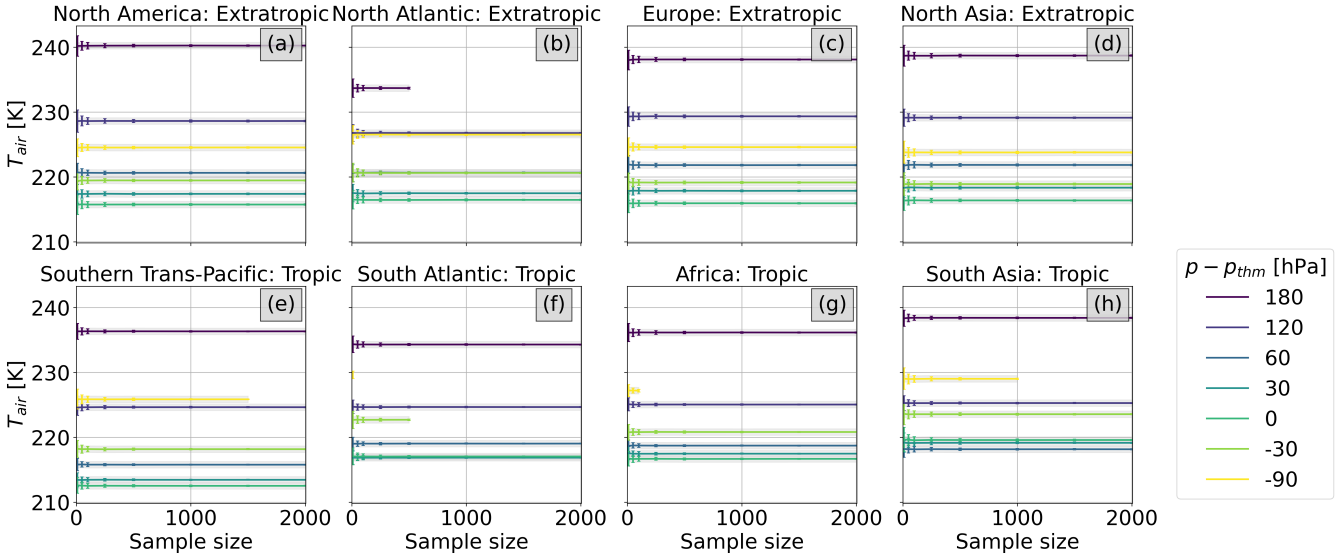

Figure S6. (a-h) Effect of sample size on IAGOS mean temperature for the different geographic regions at different vertical levels from the tropopause. Vertical lines indicate the standard deviation from the mean and grey shading shows the accuracy of the IAGOS ICH sensor for temperature. For each sample size, 1000 tests were drawn.

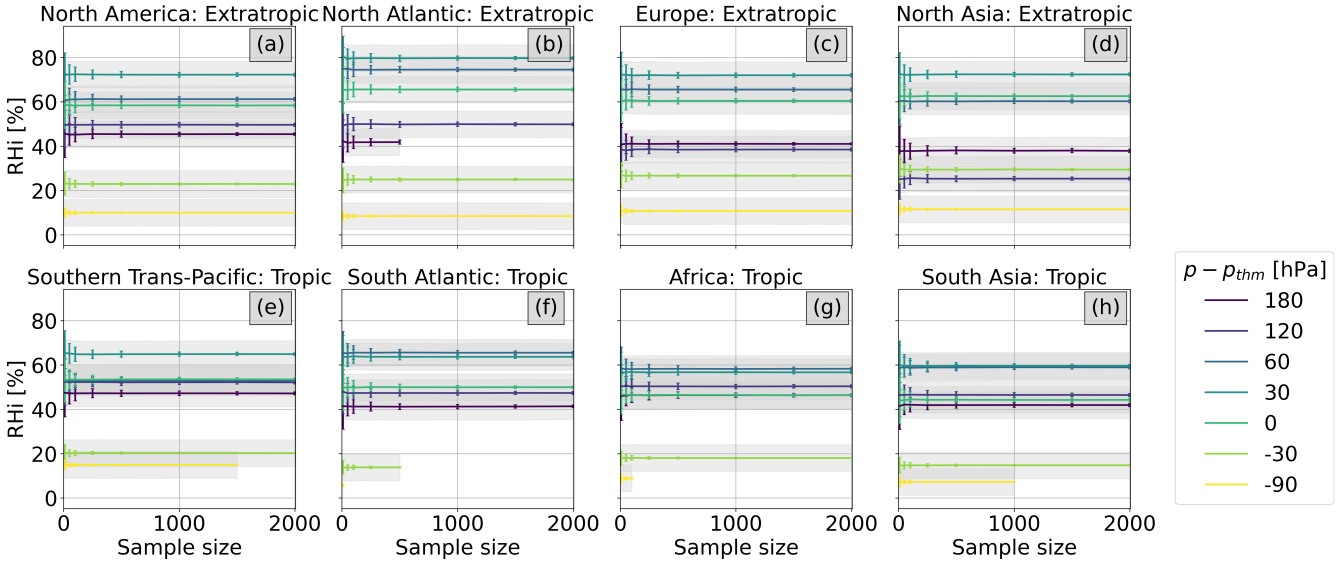

Figure S7. (a-h) Effect of sample size on IAGOS mean relative humidity over ice for the different geographic regions at different vertical levels from the tropopause. Vertical lines indicate the standard deviation from the mean and grey shading shows the accuracy of the IAGOS ICH sensor for relative humidity. For each sample size, 1000 tests were drawn.

The effect of the sample size on the ISSR fraction is shown in Fig. S8. It is important to investigate this as the ISSR fraction is a fraction of the number of points that show ISS to the total number of points available for the given conditions. We also see this sensitivity in Fig. S8. The mean ISSR fraction appears to stabilise already at around 250 samples, in which the standard deviation is between 2% and 2.5%, approximately. Given the natural variability of ISSRs, this is not statistically significant.

Furthermore, as the number of samples increases, we do not see a large impact on the reduction of the standard deviation; generally, the change in the standard deviation is less than 1% going from 250 to 500 samples. Therefore, 250 to 500 samples is considered sufficient.

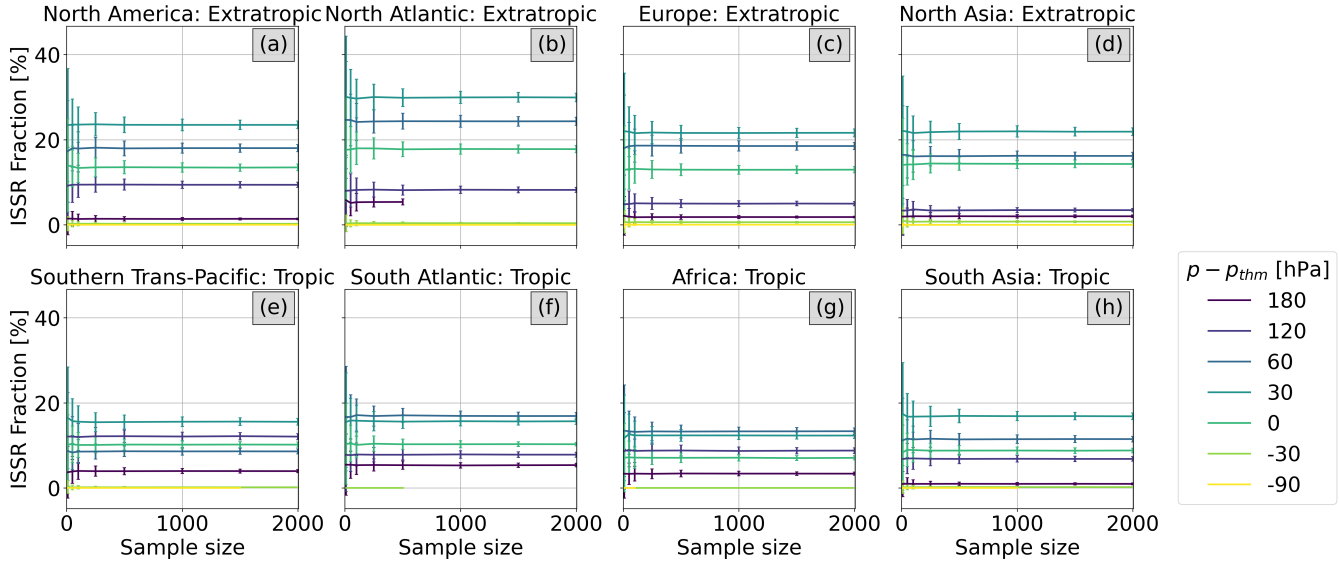

Figure S8. (a-h) Effect of sample size on IAGOS ice supersaturated region fraction for the different geographic regions at different vertical levels from the tropopause. Vertical lines indicate the standard deviation from the mean. For each sample size, 1000 tests were drawn.

We also analyse the effect of sample size on the ETS, shown in Fig. S9. However, in this case, we only take 100 tests per sample size for each region and vertical level combination due to the time it takes to calculate the ETS. The mean ETS seems to stabilise around 250 to 500, meanwhile the standard deviation first appears to stabilise between 500 and 1000 samples. However, in the lower stratosphere, the stabilisation occurs close to 1000 samples. At 250 samples, the 95% confidence interval has already reduced significantly for all vertical levels except for in the lower stratosphere. Here, the 95% confidence interval with 250 samples is approximately 0.015, which is still small, but is also dependent on the region. Hence, for the analysis of the ETS, we also recommended using at least 250 to 500 samples, but a larger sample size would result in less variation of the ETS.

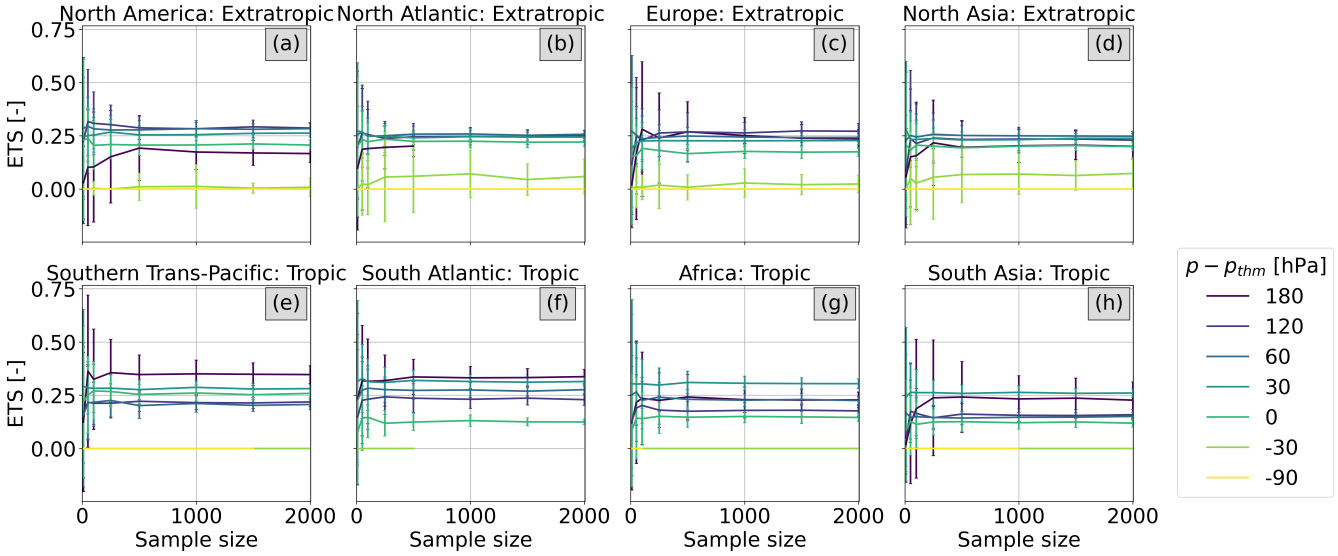

Figure S9. (a-h) Effect of sample size on the equitable threat score (ETS) for the different geographic regions at different vertical levels from the tropopause. Vertical lines indicate the standard deviation from the mean. Shading shows the 95% confidence interval. For each sample size, 100 tests were drawn.

S3 Distribution of differences in temperature and relative humidity over ice between IAGOS and ERA5

Here, we present the distribution of the differences in temperature and RHi between IAGOS and ERA5. The differences in temperature are displayed in Fig. S10. The differences in RHi are displayed in Fig. S11.

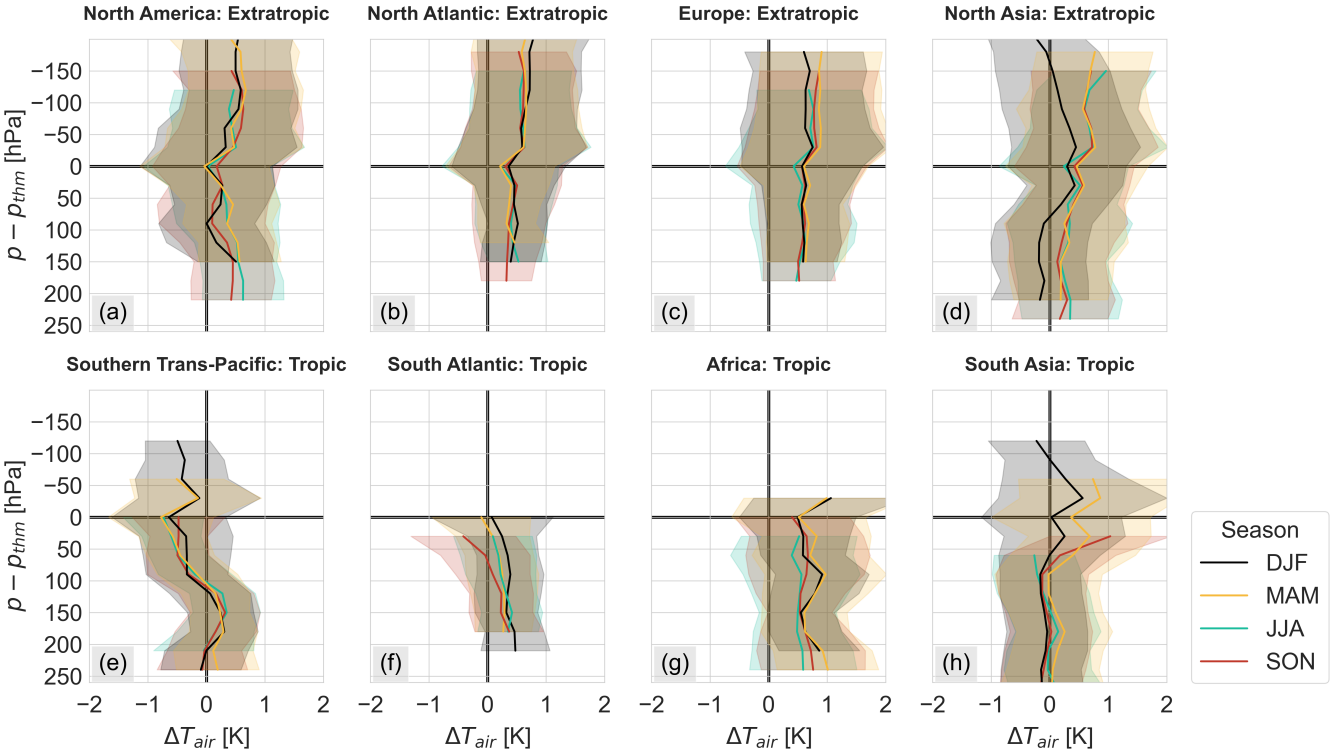

Figure S10. (a-h) Vertical distribution of temperature differences between IAGOS and ERA5 ($\Delta T = T_{\text{IAGOS}} - T_{\text{ERA5}}$) per season and per region, using levels based on distance to thermal tropopause, only considering levels with 500+ samples. Shading shows $\pm$ 1 standard deviation around the mean difference.

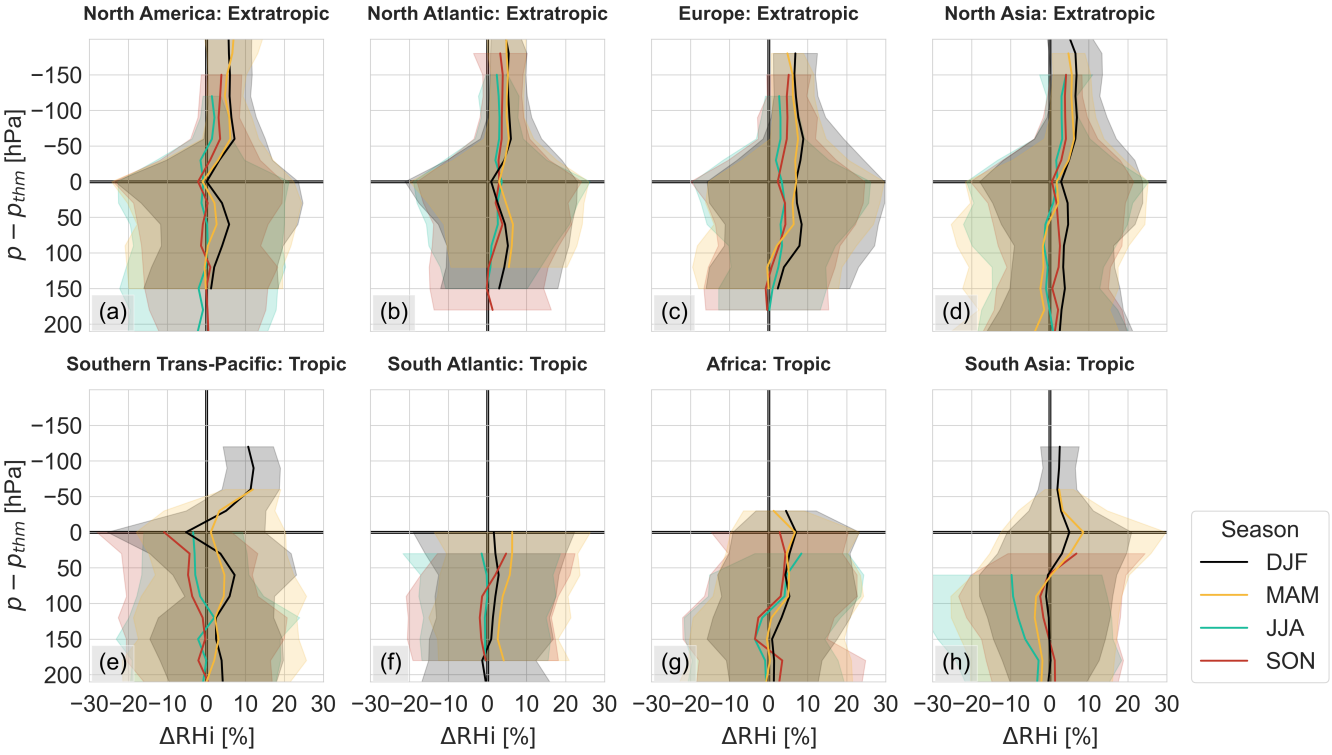

Figure S11. (a-h) Vertical distribution of relative humidity over ice differences between IAGOS and ERA5 ($\Delta\text{RHi} = \text{RHi}_{\text{IAGOS}} - \text{RHi}_{\text{ERA5}}$) per season and per region, using levels based on distance to thermal tropopause, only considering levels with 500+ samples. Shading shows $\pm$ 1 standard deviation around the mean difference.

S4 Frequency of cloudy conditions per season

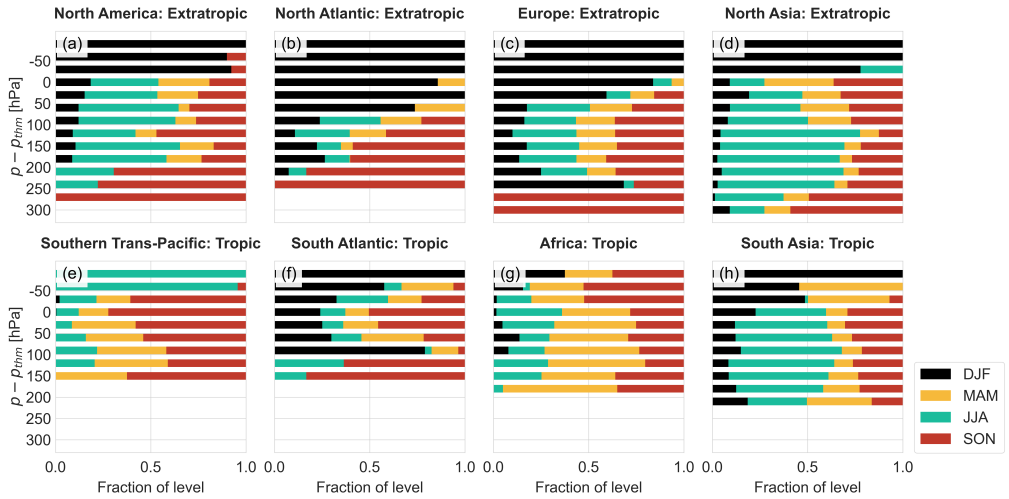

Figure S12. (a-h) Fraction of cloudy conditions for each season per layer and geographic region, based on IAGOS measurements using the ice crystal number concentration to classify a point as in cloud.

S5 Ice supersaturated region equitable threat score different ERA5 RHi thresholds in MAM and SON

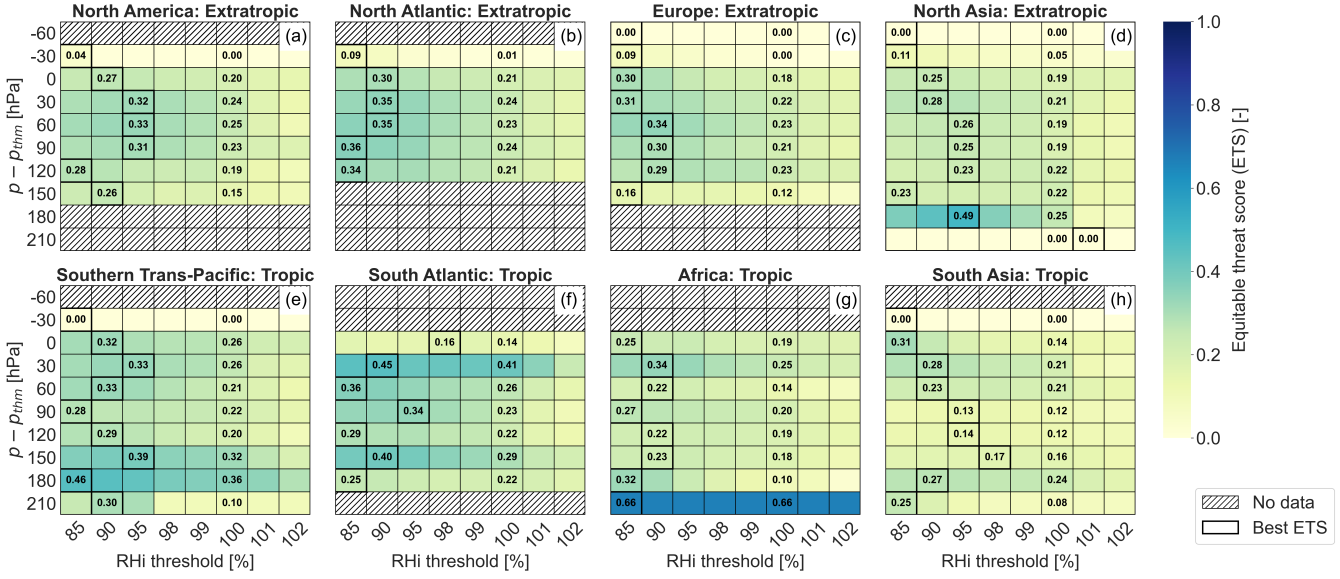

Figure S13. (a-h) Vertical distribution of ice supersaturated region equitable threat score per geographical region for different ERA5 RHi thresholds in MAM. ETS is calculated for level, season and region for which there are 500+ samples.

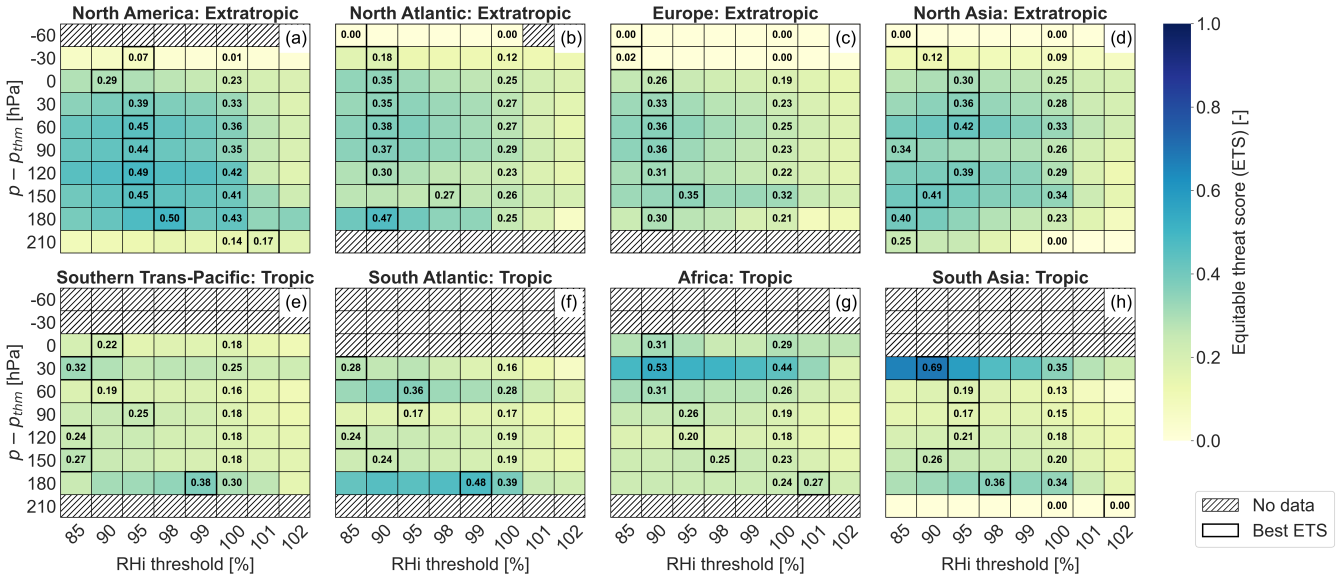

Figure S14. (a-h) Vertical distribution of ice supersaturated region equitable threat score per geographical region for different ERA5 RHi thresholds in SON. ETS is calculated for level, season and region for which there are 500+ samples.

S6 Ice supersaturated region equitable threat score different ERA5 RHi thresholds in indeterminate conditions

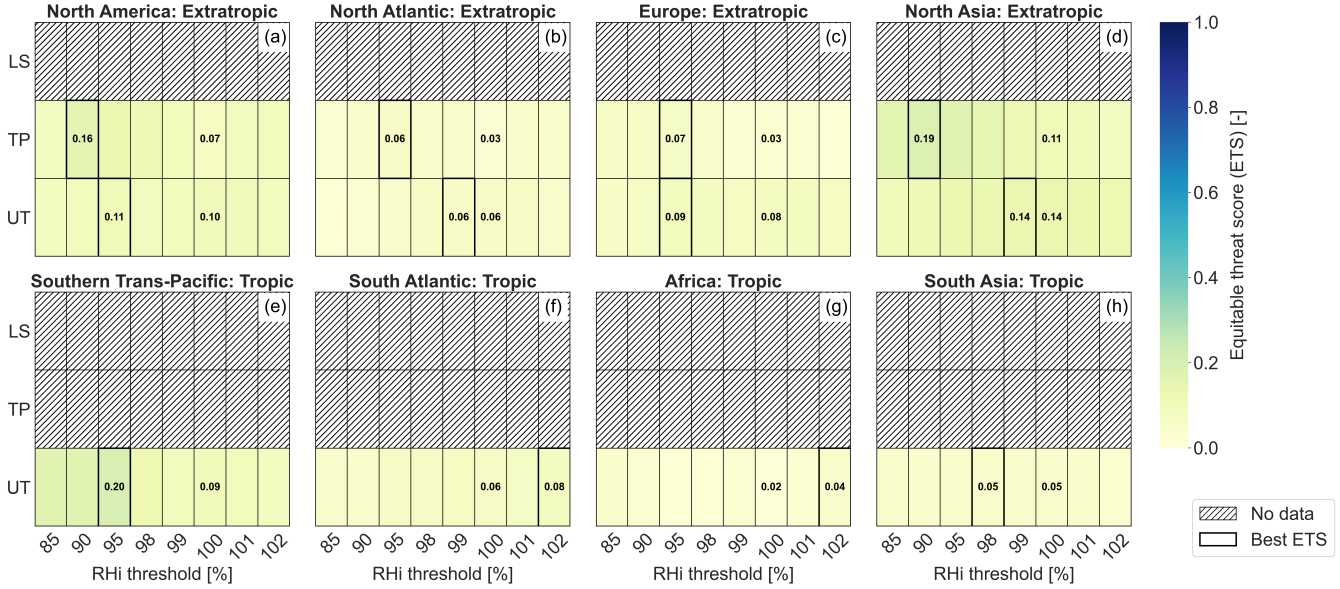

Figure S15. (a-h) Ice supersaturated region equitable threat score under indeterminate conditions for different ERA5 RHi thresholds in the upper troposphere (UT), tropopause (TP) and the lower stratosphere (LS). The different conditions have been matched between IAGOS and ERA5. Only combinations with 250+ samples are considered.

S7 North Atlantic weather pattern classification

The North Atlantic weather patterns are determined using the classification presented by Irvine et al. (2013), which is based on the similarity of the daily mean geopotential height anomaly to typical patterns, i.e. the North Atlantic Oscillation (NAO) and East Atlantic (EA) patterns. The daily mean geopotential height is obtained from the Copernicus Climate Data Store (CDS) (Hersbach et al., 2023) at a pressure level of 250 hPa. Subsequently, the anomalies with respect to the entire period 2011-2022 are calculated. Days are then assigned to five winter weather patterns (W1-W5) and three summer weather patterns (S1-S3), according to a set of criteria (Irvine et al., 2013). The characteristics of these weather patterns can be found in Table S1. The vertical distribution of the frequency of the winter and summer weather patterns is presented in Fig. S16.

Table S1. North Atlantic weather pattern characteristics for winter (W1-W5) and summer (S1-S3) (Irvine et al., 2013).

Type	Pattern	Jet stream position	Jet stream strength
W1	EA+	Zonal	Strong
W2	NAO+	Tilted	Strong
W3	EA-	Tilted	Weak
W4	NAO-	Confined	Strong
W5	Mixed	Confined	Weak
S1	EA+	Zonal	Strong
S2	Mixed	Weakly tilted	Weak
S3	EA-	Strongly tilted	Weak

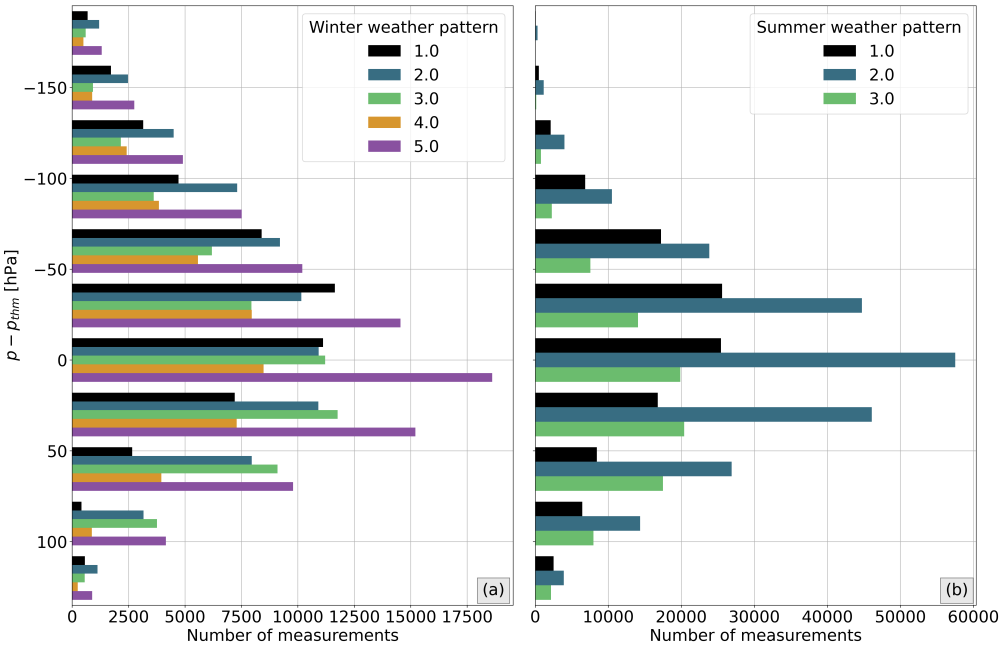

Figure S16. Vertical distribution with respect to the thermal tropopause of the number of measurements within each **(a)** winter and **(b)** summer weather pattern

Using ERA-interim, Irvine et al. (2012) found that there is a dependency of ice supersaturated region occurrence on different North Atlantic weather patterns. We explore if they also have an impact on the biases to expect in ERA5. We consider eastbound

and westbound routes separately as eastbound routes tend to take advantage of the jet stream to reduce fuel consumption. The vertical distribution of ISSR fraction for the winter and summer weather patterns on eastbound and westbound routes are shown in Fig. S17 and Fig. S18, respectively. No differences in the ISSR fraction are found between the summer weather patterns, both on eastbound and westbound routes. The summer patterns are also weaker than the winter weather patterns due to weaker teleconnection patterns and less variation of the jet stream latitude (Irvine et al., 2013). With regard to the winter weather patterns, we see a clear distinction in the ISSR fraction on westbound routes; winter weather pattern 2 and 3 show lower ISSR fractions compared to winter weather pattern 1, 4 and 5. The difference is that the jet steam position of pattern 2 and 3 is tilted, whereas winter weather pattern 1 is zonal, and 4 and 5 are confined.

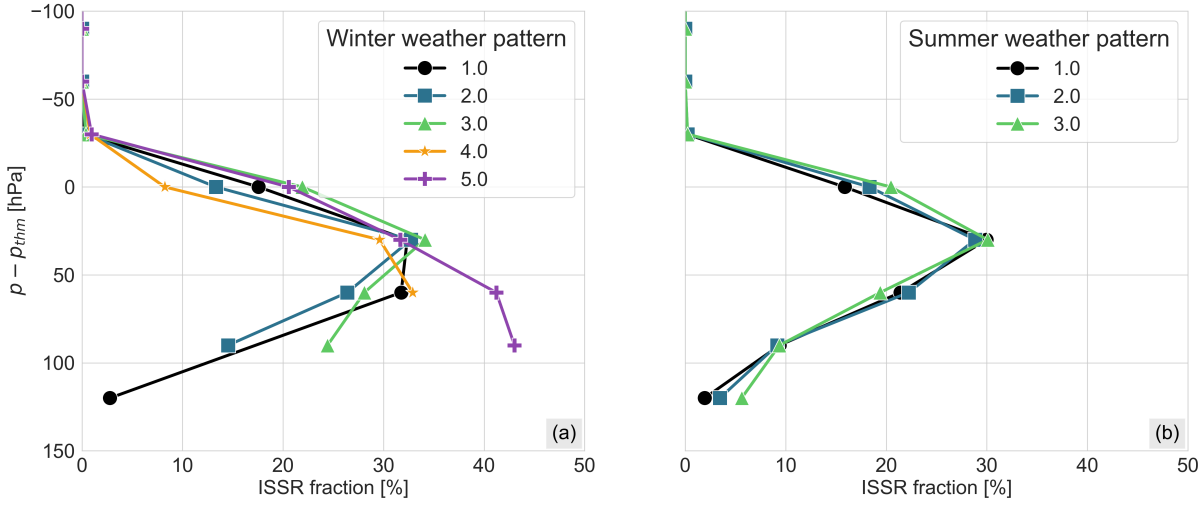

Figure S17. Vertical distribution of IAGOS ISSR fraction on eastbound routes over the North Atlantic for **a)** winter and **b)** summer weather patterns. Only combinations of weather pattern and vertical level with 250+ samples are considered.

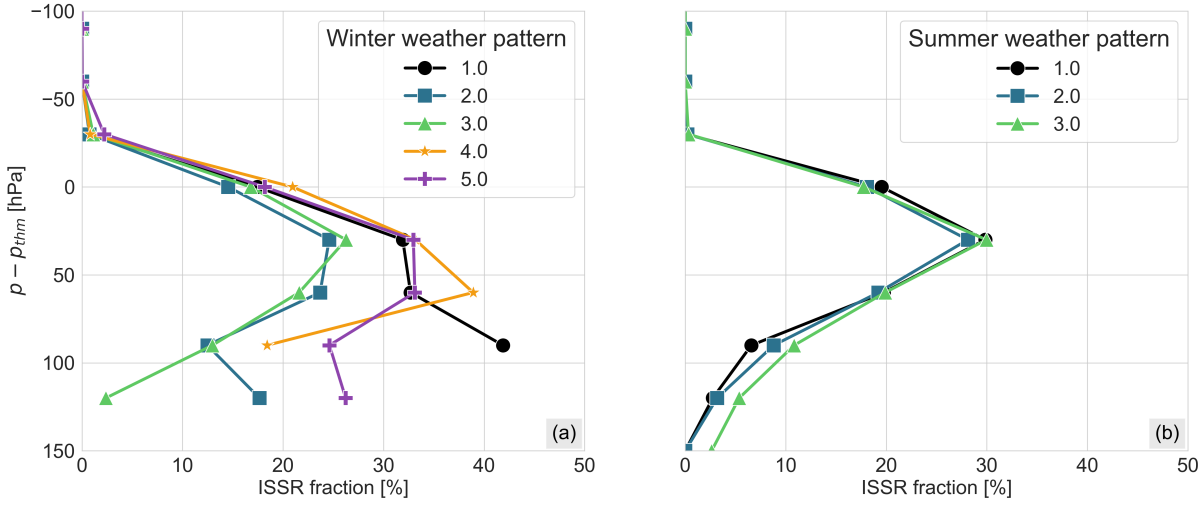

Figure S18. Vertical distribution of IAGOS ISSR fraction on westbound routes over the North Atlantic for **a)** winter and **b)** summer weather patterns. Only combinations of weather pattern and vertical level with 250+ samples are considered.

When comparing the ETS between eastbound and westbound routes, we observe more differences between the winter weather patterns on eastbound routes, as seen in Fig. S19 and Fig. S20. However, westbound routes show a higher ETS than eastbound routes, but also have a lower ISSR fraction, particularly for winter weather pattern 1 and 2. These differences in the ETS could be related to the spatial distribution of ISSRs that result from each winter weather pattern type. For example, the distribution of ISSRs may be more patchy close to and along the jet stream, but larger ISSRs are found further from the jet stream, which ERA5 may be better able to predict. Irvine et al. (2012) showed different distributions and frequencies of ISSRs in ERA-Interim for the different winter weather patterns. Moreover, a less patchy area of high ISSR frequency was found over Greenland than along the jet stream. This was obtained by averaging over several winters, thus we cannot identify if the larger areas are due to averaging or if larger areas of ISSRs occur at more northern latitudes.

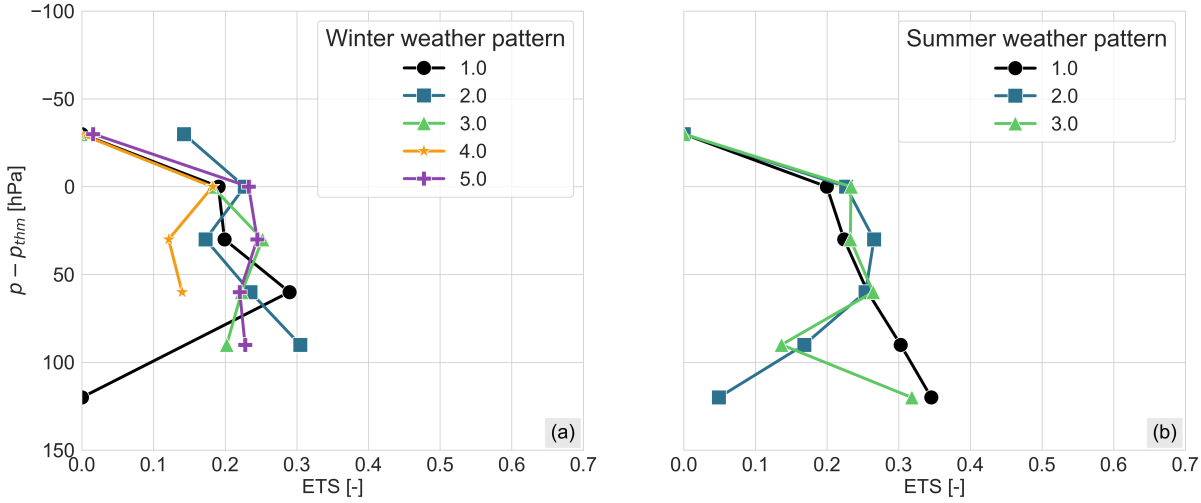

Figure S19. Vertical distribution of ETS from prediction of ISSRs in ERA5 on eastbound routes over the North Atlantic for **a)** winter and **b)** summer weather patterns. Only combinations of weather pattern and vertical level with 250+ samples are considered.

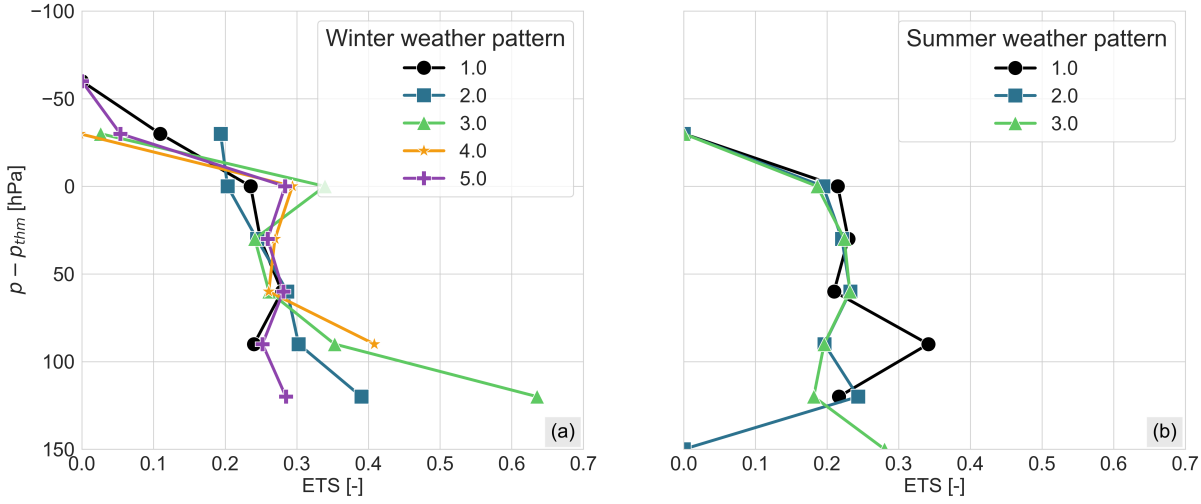

Figure S20. Vertical distribution of ETS from prediction of ISSRs in ERA5 on westbound routes over the North Atlantic for **a)** winter and **b)** summer weather patterns. Only combinations of weather pattern and vertical level with 250+ samples are considered.

References

Hersbach, H., Bell, B., Berrisford, P., Horányi, A., Sabater, J. M., Nicolas, J., Peubey, C., Radu, R., Rozum, I., Schepers, D., Simmons, A., Soci, C., Dee, D., and Thépaut, J.-N.: ERA5 monthly averaged data on single levels from 1940 to present. Copernicus Climate Change Service (C3S) Climate Data Store (CDS), https://doi.org/10.24381/cds.f17050d7, (last access: 2024-12-10), 2023.

Irvine, E. A., Hoskins, B. J., and Shine, K. P.: The dependence of contrail formation on the weather pattern and altitude in the North Atlantic, Geophysical Research Letters, 39, https://doi.org/10.1029/2012GL051909, 2012.

Irvine, E. A., Hoskins, B. J., Shine, K. P., Lunnona, R. W., and Froemming, C.: Characterizing North Atlantic weather patterns for climate-optimal aircraft routing, Meteorological Applications, 20, https://doi.org/10.1002/met.1291, 2013.

Johnson, R. W.: An Introduction to the Bootstrap, Teaching Statistics, 23, 49–54, https://doi.org/10.1111/1467-9639.00050, 2001.

Petzold, A., Khan, N. F., Li, Y., Spichtinger, P., Rohs, S., Crewell, S., Wahner, A., and Krämer, M.: Most long-lived contrails form within cirrus clouds with uncertain climate impact, Nature Communications, 16, 9695, https://doi.org/10.1038/s41467-025-65532-2, 2025.

Sanogo, S., Boucher, O., Bellouin, N., Borella, A., Wolf, K., and Rohs, S.: Variability in the properties of the distribution of the relative humidity with respect to ice: implications for contrail formation, Atmospheric Chemistry and Physics, 24, 5495–5511, https://doi.org/10.5194/acp-24-5495-2024, 2024.

Wang, Z., Bugliaro, L., Gierens, K., Hegglin, M. I., Rohs, S., Petzold, A., Kaufmann, S., and Voigt, C.: Machine learning for improvement of upper-tropospheric relative humidity in ERA5 weather model data, Atmospheric Chemistry and Physics, 25, 2845–2861, https://doi.org/10.5194/acp-25-2845-2025, 2025.

Wolf, K., Bellouin, N., Boucher, O., Rohs, S., and Li, Y.: Correction of ERA5 temperature and relative humidity biases by bivariate quantile mapping for contrail formation analysis, Atmospheric Chemistry and Physics, 25, 157–181, https://doi.org/10.5194/acp-25-157-2025, 2025.